Nanoscale

Chiral Nanohole Arrays

Journal:	*Nanoscale*
Manuscript ID	NR-ART-11-2019-009722.R2
Article Type:	Paper
Date Submitted by the Author:	12-Nov-2019
Complete List of Authors:	Ai, Bin; Chongqing University, School of Microelectronics and Communication Engineering; Chongqing Key Laboratory of Bio perception & Intelligent Information Processing Luong, Hoang; University of Georgia, Department of Physics and Astronomy Zhao, Yiping; University of Georgia, Department of Physics and Astronomy

Chiral Nanohole Arrays

Bin Ai,[†*] *Hoang M Luong*,[†] *Yiping Zhao*

[†] These authors contribute equally to this work

Prof. B. Ai,
School of Microelectronics and Communication Engineering, Chongqing University, Chongqing 400044, China
Chongqing Key Laboratory of Bio perception & Intelligent Information Processing
19 Chongqing, P.R. China, 400044
H.M. Luong, Prof. Y. Zhao
Department of Physics and Astronomy, University of Georgia, Athens, Georgia 30602, United States
Email: binai@cqu.edu.cn

Keywords: nanoholes, chiral metamaterials, plasmonic sensors, colloidal lithography, Born−Kuhn model

Chiral nanohole array (CNA) films are fabricated by a simple and efficient shadow sphere lithography (SSL) method and achieve label-free enantiodiscrimination of biomolecules and drug molecules at the picogram level. The intrinsic mirror symmetry of the structure is broken by three subsequent depositions onto non-close packed nanosphere monolayers with different polar and azimuthal angles. Giant chiro-optical responses with a transmission as high as 45 %, a chirality of 21 °/μm, and a *g*-factor of 0.17, respectively, are generated, which are among the largest values that have been reported in literature. Such properties are due to the local rotating current density generated by surface plasmon polariton as well as strong local rotating field produced by localized surface plasmon resonance, which leads to the excitation of substantial local superchiral fields. The 70 nm-thick CNAs can achieve label-free enantiodiscrimination of

biomolecules and drug molecules at the picogram level as demonstrated experimentally. All these advantages make the CNAs ready for low-cost, high-performance, and ultracompact polarization converters and label-free chiral sensors.

1. Introduction

Chiral metamaterials (CMs) are artificial structures that cannot be superposed with their mirror images. Their structural chirality often leads to different interactions with left-handed circularly polarized (LCP) and right-handed circularly polarized (RCP) light, induces a rotation in polarization direction of light (known as circular birefringence or optical rotation), and causes different absorbance (known as circular dichroism (CD)).[1] Compared to natural chiral molecules, like DNA and proteins, the CMs can significantly improve the CD response by orders of magnitude.[2-4] Moreover, the CMs can be artificially designed with robust tunability and flexibility, thus gained great attentions in applications for negative refraction,[5, 6] light polarization manipulation,[7-11] controlled CD switching,[12, 13] second-harmonic generation,[14, 15] superchiral field based biosensing,[16-19] *etc*.

To advance the applications of CMs, strong chiroptical effects as well as simple and scalable fabrication techniques are always the two important goals. In principle, two types of CMs, with elements of truly three-dimensional (3D) chiral shapes [20-23] and the two-dimensional (2D) planar structures,[24-28] are developed. 3D CMs, like stacked unit cells[29-31] and helices,[7, 32, 33] usually possess strong chiroptical effects due to their large gyratory coefficient. However, the fabrication

of 3D CMs mainly relies on electron beam lithography (EBL)[34] and direct laser writing (DLW),[35] These processes are time-consuming, expensive, and not suitable for scalable fabrication, or lacks the high resolution of EBL and cannot produce chiral structures with feature size small enough to show optical activity in the visible wavelength region. 3D CMs can also be realized by attaching metal nanoparticles on 3D chiral scaffolds such as macromolecules[36-38] and block copolymers.[39, 40] These methods are low-cost and scalable, but the obtained chiroptical properties are usually much weaker than those fabricated by EBL and DWL. Furthermore, complicated 3D CMs such as chiral hollow nanocone arrays,[41] stacked patches on nanospheres,[21, 42] and Swiss-roll structures,[43] have also been realized by a templated based glancing angle deposition (GLAD) method.

2D planar CMs have unit cells that lack the in-plane mirror symmetry but possess the reflection symmetry with respect to the structural plane. Compared to 3D CMs, the 2D CMs bear many technological advantages, such as easy fabrication and ultracompact on-chip integration. For this reason, significant efforts have been devoted to the development of 2D CMs. Structures like gammadions,[16, 44] shurikens,[45] chiral arranged nanoparticles,[24, 46] L-shaped,[27] G-shaped,[47] and S-shaped[48] patterns, have been realized and their chiro-optical properties have been demonstrated. In fact, these 2D CMs do not exhibit optical activity due to the mirror symmetry and reciprocity.[44] The reported optical activity is resulted from broken mirror symmetry due to the index mismatch at the top and bottom interfaces, and the chiro-optical response is much weaker than that of 3D CMs. In order to produce stronger chiro-optical response in 2D CMs, a

natural strategy is to break the structure's mirror symmetry by a moderate shape modification of metal elements, like the elevating starfish metamaterials.[49] The other strategy is to excite both propagating surface plasmon polariton (SPP) and localized surface plasmon resonance (LSPR) in periodic chiral metamaterials, which has been demonstrated by gammadion nanohole arrays (NAs).[50] Based on above two strategies, swirl NAs[51] and ultrathin moiré patterns [52, 53] were designed, and their chiro-optical response were comparable with that of 3D CMs. In the meantime, high optical transmissions were obtained due to the well-known extraordinary optical transmission effect (EOT) in perforated metallic films.[54, 55] The high transmission, *i.e.*, low optical loss, is vital for facilitating prospective applications. However, for the achiral NAs, in order to obtain the chiro-optical response, the light incident angle could not be zero which makes the measurement complicated, and further work applying these structures to pursue higher chiral performance and explore their applications is scarce. In addition, most of the 2D CMs were also fabricated by EBL or focused ion beam (FIB).[56] The fabrication processes are still of low throughput and poor scalability. Though efficient soft lithography techniques were used for stacked NAs,[52, 53] they still require multiple steps of etchings, transferring, and precise alignment. Thus, it remains a big challenge to produce 2D chiral metamaterials with strong chiro-optical responses using a simple fabrication process, especially for applications in ultracompact devices and high transmission.

Here, ultrathin chiral nanohole arrays (CNAs) are fabricated by a shadow sphere lithography technique (SSL).[57] Ag is deposited on non-closed nanosphere monolayers subsequently with

three different polar and azimuthal angles, introducing the structural chiral characteristic. The fabrication method is simple and capable of patterning large surface areas in parallel at low cost, yet with good control of the main structural parameters. The resulting CNA structures not only lack the in-plane mirror symmetry, but also break the mirror symmetry in light propagation direction. Both SPP and LSPR are excited inside the holes by the structural periodic grating and at the hole edge, respectively. The local rotating current density is generated due to SPP and the asymmetry in light propagation direction, while strong local rotating field is produced due to LSPR and the structural mirror symmetry broken. When the handedness of the helical rotating current is the same as that of the polarized light, higher transmission is obtained, and *vice versa*, which produces a giant chiro-optical response, with a transmission as high as 45 %, a chirality of 21 °/μm, and a *g*-factor of 0.17, respectively, which are among the largest values that have been reported so far.[41, 52, 53, 58] The strong superchiral fields excited in the nanoholes can achieve label-free enantiodiscrimination of biomolecules and drug molecules at the picogram level as demonstrated experimentally. The CNAs with the simple fabrication process, strong chirality, high sensitivity to chiral molecules, high transmission, and ultrathin thickness are promising for low-cost, high-performance, and ultracompact on-chip applications, such as polarization converters and chiral sensors.

2. Results and Discussion

2.1 Design and Theoretic Concept

The CNAs are designed based on NAs which have the following unique properties: 1) the

EOT effect: the optical transmission in the plasmon-grating coupling wavelength region can be much greater than that predicted by Bethe's theory; 2) coexistence of SPP and LSPR: both could be used to generate giant chiro-optical response; and 3) ultra-thin thickness. The interaction between surface plasmon and light can be controlled by many factors, like the shape and dimension of hole aperture, film thickness, periodicity, lattice symmetry, filling factor of the NA, incident angle of light, and the dielectric constant of the metal. This large tunable parameter space makes the design of NA-based CMs more flexible. A good NA-based CM design should have a NA unit cell with intrinsic mirror symmetry breaking, break the mirror symmetry in light propagation direction, and have the flexibility to produce strong chirality. The proposed CNAs fabrication strategy by SSL is shown in **Figure 1**. Hexagonal non-close-packed nanosphere (period P = 500 nm, diameter d = 200 nm) monolayers are used as a template. Ag is then subsequently deposited at different incident and azimuthal angles, $\theta_1 = 10°$ and $\varphi_1 = 0°$, $\theta_2 = 20°$ and $\varphi_2 = \pm 120°$, and $\theta_3 = 30°$ and $\varphi_3 = \pm 240°$, respectively. Here θ_1, θ_2, and θ_3 are the vapor incident angles with respect to substrate normal, φ_1, φ_2, and φ_3 are the projected azimuthal angle of incident vapor on the monolayer plane, and "±" represents the counter-clockwise/clockwise (CCW/CW) azimuthal rotation of the substrate. We denote CCW and CW CNAs as left-handed CNAs (LH-CNAs) and right-handed CNAs (RH-CNAs), respectively. The initial φ_1 is chosen arbitrarily. After removing the nanosphere monolayer, CNAs are left on the substrates. The bottom panel in **Figure 1A** shows the morphology of one unit-cell of such a structure predicted using our in-house MATLAB program. The thickness of each Ag deposition is set to be t = 30

nm. clearly, the structures are formed by stacking three oval nanoholes with increasing aspect ratio (**Figure S1**). The distance l between the hole edge and the center of the original nanospheres (**Figure 1A**) increase with θ by $l = \frac{d}{2} \times \tan\left(45 + \frac{\theta}{2}\right)$, for example, l_1 (red) = 119 nm, l_2 (yellow) = 143 nm, and l_3 (blue) = 173 nm, respectively, showing the breaking in-plane mirror symmetry. The hole shape and area also change step-wisely and monotonically with film thickness (**Figure S1**), which breaks the mirror symmetry in light propagation direction. Thus, the proposed CNAs have truly chiral shapes, *i.e.*, intrinsic mirror asymmetry, while the thickness is also ultrathin.

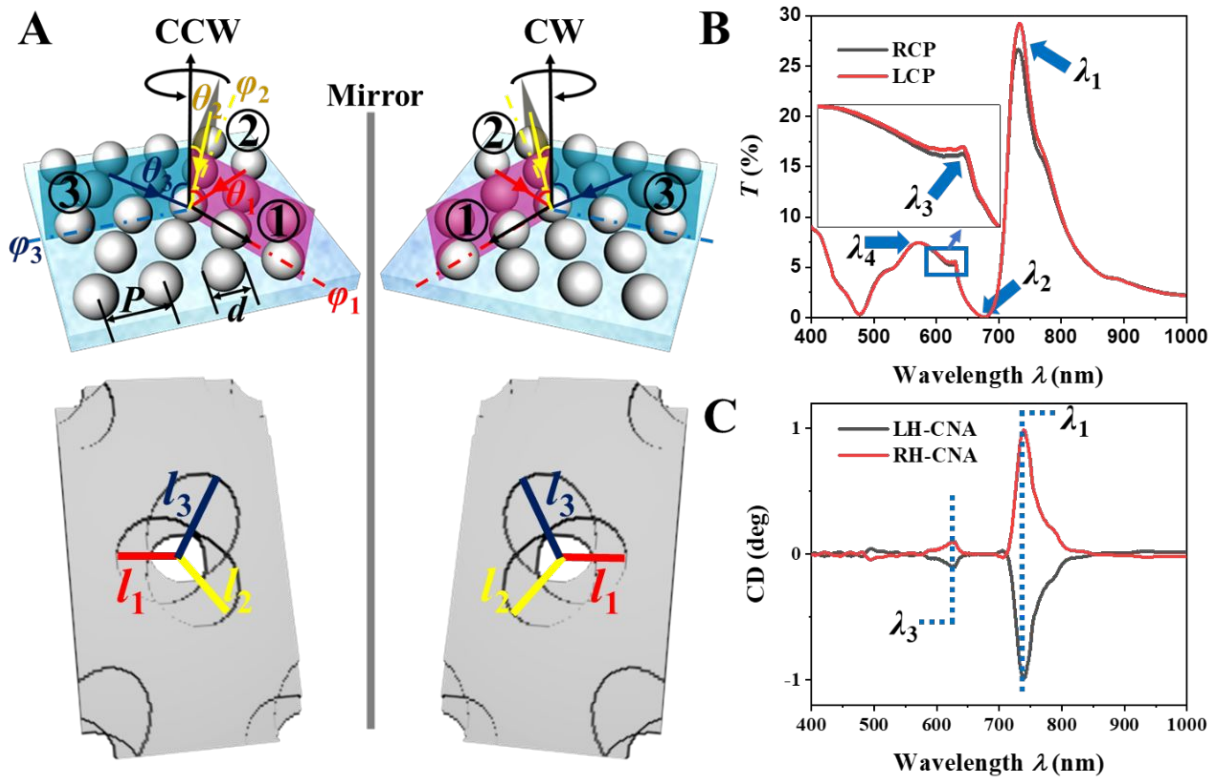

Figure 1. (A) Top panel: schematics of the fabrication process and the main parameters of polar angle θ, azimuthal angle φ, period P, and diameter of the etched sphere d. Bottom panel:

Calculated structures of the CNAs based on an in-house MATLAB program. (B) The calculated $T_R(\lambda)$ and $T_L(\lambda)$ of a LH-CNA. (C) The calculated CD spectra of a LH-CNA and a RH-CNA.

The optical property of the proposed CNAs can be predicted by FDTD calculations. **Figure 1B** shows the calculated polarized RCP and LCP transmission spectra $T_R(\lambda)$ and $T_L(\lambda)$ of the LH-CNA using the bottom-left model in **Figure 1A**. For both $T_R(\lambda)$ and $T_L(\lambda)$, the peaks/valleys at $\lambda_1 \approx 734$ nm, $\lambda_2 = 678$ nm, $\lambda_3 = 630$ nm, and $\lambda_4 = 571$ nm can be assigned to the (1,0) Ag/glass SPP resonance peak, (1,0) Ag/glass Wood's anomaly transmission minima,[59] (1,1) Ag/glass SPP resonance peak, and (1,0) Ag/air SPP resonance peak, respectively.[60] A clear chiro-optical response (difference in the RCP and LCP transmission spectra) is observed at the two SPP peaks λ_1 and λ_3, though the position and width of these two peaks are independent of the polarization of the incident light. The magnitude of $T_R(\lambda)$ and $T_L(\lambda)$ at $\lambda_2 = 678$ nm and $\lambda_4 = 571$ nm is the same because the Woods anomaly only depends on the period and interfacial material property, not the topological shape of the holes, and the resonance at λ_4 is too weak to induce the chiro-optical response due to the low refractive index of air. **Figure 1C** plots the differential CD spectra according to the definition $CD(\lambda) = 32.98° \times [T_R(\lambda) - T_L(\lambda)]$[52, 53] of the LH-CNA and corresponding RH-CNA structures. The two CD spectra show exact the opposite response to RCP and LCP incident lights, indicating them are true enantiomer. For the LH-CNA/RH-CNA structure, a sharp peak/valley is observed exactly at $\lambda_1 = 739$ nm, *i.e.*, the (1,0) Ag/glass SPP resonance wavelength, and a relatively weak peak/valley appears at $\lambda_3 = 630$ nm, the (1,1)

Ag/glass SPP resonance wavelength. The chiro-optical response of the proposed LH-CNA and RH-CNA structures are due to the difference in the induced chiral current density distribution under the LCP and RCP incidence, see discussion in **Section SII** in **Supporting Information** (**SI**). Through the MATLAB prediction of the structure and calculated spectra, the CNAs designed by the simple shadowing growth process is promising to show significant chiro-optical responses.

2.2 Experimental CNAs

Experimentally, the CNAs were fabricated according to the design and parameters mentioned in **Figure 1A**. **Figure 2A** shows a representative atomic force microscope (AFM) image of a LH-CNA. Three oval nanoholes as shown in **Figure 2B**, with the measured $l_1 = 130 \pm 10$ nm, $l_2 = 150 \pm 20$ nm, and $l_3 = 180 \pm 20$ nm, are stacked subsequently, as indicated by the colored outlines in **Figure 2A**, leading to the mirror symmetry breaking. Although the Ag thickness of each layer was set to be 30 nm, the actual total thickness t of the CNAs was around 70 nm because it was an oblique deposition. The thickness of the three stacked Ag thin layers in the nanohole is determined to be $t_1 = 22 \pm 2$ nm, $t_2 = 45 \pm 4$ nm, and $t_3 = 53 \pm 5$ nm, respectively, as shown in **Figure 2C**. Thus, a spiral staircase from the substrate to the top Ag layer appears in the nanoholes, thus breaks the mirror symmetry in light propagation direction. **Figure 2D** shows a representative AFM image of a corresponding RH-CNA fabricated under the same condition, except that the azimuthal rotation direction was opposite to that of the LH-CNA. The RH-CNA shows the exactly mirror-inverted structures to that of the LH-CNA. Compared to the models

described in **Figure 1A**, the experimental patterns and those predicted by the MATLAB program are in qualitative agreement. However, there are morphology differences in detailed features, such as in the experimental samples, the surfaces are rough, the slopes of hole edge and the transition of each layer are much smaller, and *l* in each layer is a little larger. We expect that these differences could cause different optical response of the experimental samples compared to that of FDTD.

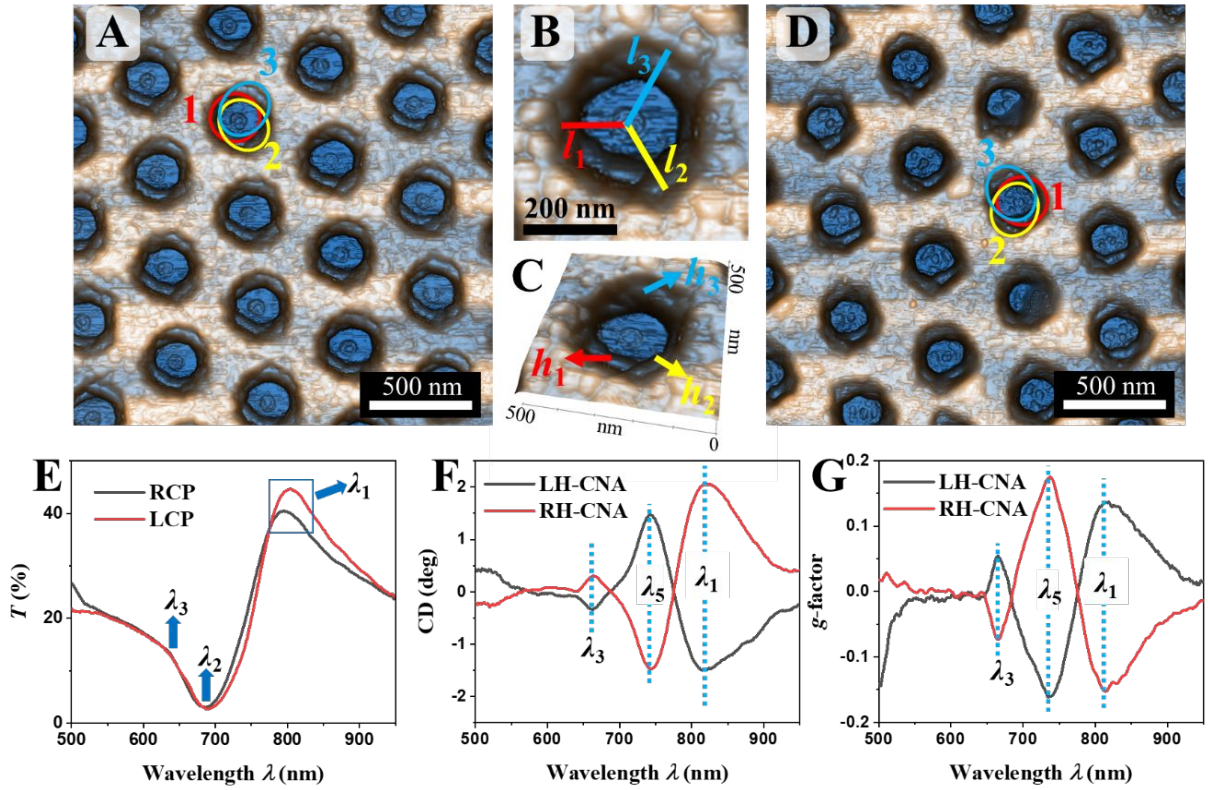

Figure 2. (A) Representative top-view AFM image of a LH-CNA. (B) The top-view and (C) 3D AFM images of one chiral nanohole. (A) Representative top-view AFM image of a RH-CNA. (E) Experimental $T_R(\lambda)$ and $T_L(\lambda)$ of the LH-CNA. (F) The CD spectra and (G) the *g*-factor of the LH- and RH-CNAs.

Figure 2E shows the experimental $T_R(\lambda)$ and $T_L(\lambda)$ of the LH-CNA. The spectra are in good quantitative agreement with the FDTD spectra, except that the positions of the resonance peaks/valleys are changed: In the experimental spectra, λ_1 is determined to be ~ 800 nm, λ_2 is ~ 685 nm, and λ_3 is ~ 630 nm, while the Ag/air SPP resonance peak λ_4 cannot be identified. The discrepancies between the experimental and FDTD spectra result mainly from the difference between the experimental samples and calculated models mentioned above. It is worth noting that in the wavelength vicinity λ_1, the $T_R(\lambda)$ and $T_L(\lambda)$ are distinctly different, which is not observed in **Figure 1B**. This indicates a clear chiro-optical response at the (1,0) Ag/glass SPP resonance. According to Refs.[61, 62], the CD spectra of the LH-CNA and the RH-CNA samples are shown in **Figure 2F**. Clearly, the CD spectral shape of the LH-CNA sample is almost exactly opposite to that of the RH-CNA sample. A significant peak (valley) occurs at λ_5 = 743 nm while a large valley (peak) appears at λ_1 = 822 nm for the LH(RH)-CNA sample. There is also a small valley (peak) emerging at λ_3 = 664 nm, which may be due to the (1,1) Ag/glass SPP resonance peak. The CD spectra remain the same independent of whether the light is incident on the front or back side of the sample, whereas are influenced by thickness of the CNAs (**Figure S3**) and angle of incident light (**Figure S4**). The quality of the chiro-optical response is characterized by two parameters, the CD ellipticity and the dissymmetry factor *g*. The CD ellipticity is relative to the total film thickness, which is defined by CD/*t*, is obtained up to 28°/μm at λ_1 = 822 nm. The dissymmetry factor *g*, which is defined as $g = \Delta A/A$, where ΔA is the differential extinction

between RCP and LCP light and A is the unpolarized extinction of the CNAs, is also calculated as shown in **Figure 2G**. The shape of the g factor spectrum is almost the inverse of the corresponding CD spectrum for each sample, and its magnitude can reach as high as 0.17 at λ_5 = 738 nm. Both the ellipticity and g-factor for the LH-CAN and RH-CAN samples are among the largest reported in the literature so far, in particular, they are higher than the corresponding values of most of 2D CMs[16, 44, 52, 58] and comparable with those of 3D CMs.[17, 28, 32, 39]

Though the calculated optical responses based on the MATLAB model (**Figures 1B** and **1C**) quantitatively agree with the experimental results (**Figure 2E** and **2F**), there are some detailed differences such as spectra shape and peak/valley locations. In order to better verify the experimental and calculated spectra, we have performed FDTD calculations based on a structure model directly extracted from the AFM images in **Figure 2A**. **Figure 3A** shows the calculated $T_L(\lambda)$ and $T_R(\lambda)$ of the LH-CNA based on the AFM model when the incident light propagates from glass substrate to Ag nanoholes. The spectral shapes of calculated $T_L(\lambda)$ and $T_R(\lambda)$ agree well with the spectra in **Figure 2E**, with well identified resonance modes $\lambda_1 \approx$ 839 nm, λ_2 = 682 nm, and λ_3 = 629 nm. The magnitude of $T_R(\lambda)$ is clearly larger than that of $T_L(\lambda)$ in the wavelength range of 730 – 770 nm, while the spectral difference at λ_1 is small. The calculated CD spectrum is shown in **Figure 3B**, and a distinguished peak at λ_5 = 764 nm and a valley at λ_1 = 855 nm are revealed, which correspond to those at λ_5 = 743 nm and λ_1 = 822 nm in **Figure 2F**, respectively, showing very strong similarity to the experimental results than that using the MATLAB model. Clearly the calculated valley of the CD spectrum at λ_1 = 855 nm is due to the

SPP plasmon mode as discussed in **Section SIII** but it is much weak compared to that in **Figure 1C**.

In order to understand the chiro-optical response, the current density distribution of different cross-cutting planes from the glass substrate (bottom) to the Ag nanohole (top) with t = 0, 15, 30, 45, 60, and 70 nm at λ_1 is calculated based on the AFM model of the LH-CNA under LCP (left panel) and RCP (right panel) and is shown in **Figure 3C**. In each plane, two current sources are visible, *i.e.*, the positive and the negative poles, labeled in **Figure 3C**. We can clearly see the pole direction pointing from the positive pole to the negative pole is changing along the propagation direction of the incident light, and this direction change is different for the LCP and RCP illuminations. As shown in **Figure 3D**, for the RCP incidence, the pole direction propagates counter-clock wisely with a final rotation angle of 30° when the light emerges from the nanohole. For the LCP incidence, the pole direction propagates clock wisely with a rotation angle of 9°. Though the relative in-plane rotation direction of the pole direction is the same as that of the polarization of the light, the emerged rotation angle is much larger for LCP incidence than that for RCP incidence. This is different from the calculation based on the MATLAB model that the pole rotation is opposite to the rotation of the incident light with RCP. The difference is due to that, compared to the MATLAB model, the sharp features in the AFM model are lost and the hole outlines become indistinguishable, which reduces the contribution of the structural handedness because the chiro-optical response at λ_1 is based on the hole outlines. Thus, the calculated valley of the CD spectrum at λ_1 = 855 nm is weaker than that in **Figure 1C**. Compared

to the experimental structures, the AFM model is usually smoother considering the AFM scanning mechanism. This makes the calculated CD response at λ_1 = 855 nm in **Figure 3B** weaker than that in **Figure 2F**.

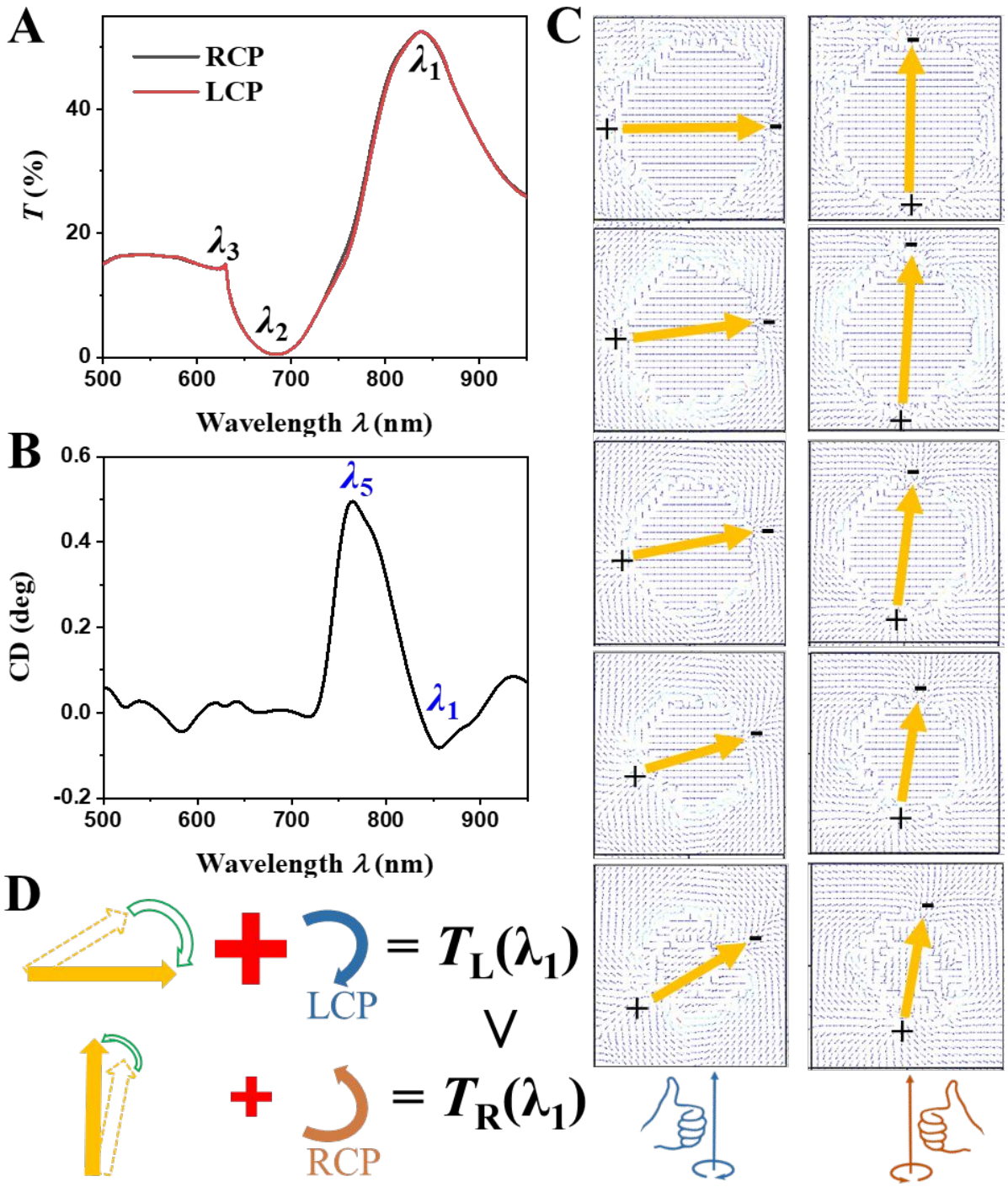

Figure 3. The calculated (A) $T_R(\lambda)$, $T_L(\lambda)$, and (B) CD(λ) of the LH-CNA based on the AFM model. (C) The local current density distributions of the LH-CNA excited by a LCP (left panel) and a RCP (right panel) incident light at λ_1 = 855 nm for the plane t = 0, 15, 30, 45, 60, and 70 nm, respectively. The arrows indicate the current density direction. (D) Top-view illustration of rotations of effective current pole directions from the bottom layer to the top layer under LCP and RCP illuminations, respectively. The straight dashed arrows represent the pole direction at the t = 0 nm plane, while the solid arrows show the pole direction at the t = 70 nm plane.

The corresponding CD peak at λ_5 = 764 nm is very strong, and its position is very close to λ_2 (= 682 nm, the (1,0) Ag/glass Wood's anomaly), we believe that such a chiro-response is due to LSPR. LSPR is confined in the vicinity of the structure surface (< 10 nm to the surface). Propagating current calculation as Figure 3 may be not good to explain the local E-fields. Thus, the localized electric field distributions $|E/E_0|$ at the interface t = 0 (Ag/glass interface), 30 nm, and 70 nm (Ag/air interface) at λ_5 = 764 nm under LCP and RCP incident lights are calculated as shown in **Figure 4**, where E is the local field and E_0 is the incident field. The vector of the E-fields is shown in the two bottom images of **Figure 4**, which evaluates the dipole orientation and indicates the propagating direction of light in the nanohole. Regardless of the polarization state of the incident light, the locations of the maximum local electric fields show a clockwise rotation along the light propagation direction. This CW rotation of the local electric fields is against the CCW rotation of the LCP electric field. This leads to a slight retardance to the evanescent field in

the non-propagating aperture. Slight twist of incident light is observed in the left bottom image in Figure 4, makes weaker energy re-emitted into freely propagating light, and lowers the transmission. While for the RCP incidence, the CW rotation of the local electric fields and RCP electric field are rotating with the same sense, which could compensate for the evanescent field, twist significantly the incident light (the right bottom image in Figure 4), and allow stronger re-emission, leading to a large transmission. The interaction between the rotated LSPR and incident light is responsible for the chiral responses. In fact, as stated before, the LH-CNA sample has spiral steps. When observing the steps along the light propagation direction in **Figure 4**, the steps twist CW, which is in-phase of the CW rotation of the local electric fields (*i.e.*, the handedness of LSPR). Such a structural handedness along the propagation direction is essential for the chiral response at λ_5 = 733 nm. In previous studies of NA-based chirality, it was claimed that LSPR could not produce significant CD.[47, 55] This conclusion is due to that their rotating trend of the local nanostructures is not definite enough to induce strong LSPR rotation in light propagation direction.

Based on the discussions of the chiro-optical response at λ_1 and λ_5, it is clear that both SPP and LSPR can "individually" induce optical activities with opposite response in one CM structure. In principle, such a chiral response could be further tuned by adjusting separation between the locations of the EOT peak and Wood's anomaly valley, *i.e.* the detailed CNA structures and periodicity. Since there are multiple EOT peaks and Wood's anomaly valleys occur in CNA structures, it is expected that there are multiple CD resonances appear, which makes the CNAs

more flexible in applications of optical devices and chiral sensing.

However, we should note that the experimental results still cannot agree with the calculation perfectly. One possible reason could be that only two- or three-unit cells were used in the calculation, while for the experimental measurement, there could be large statistical variations in the nanohole structures since the light illuminated area was larger (the diameter of the light spot was ~ 200 μm) than the single-domain area (normally in 100 × 100 μm^2). In addition, the AFM image is a convolution of the real structure and the AFM tip shape, which means the model based on AFM image still does not reflect the true structure.

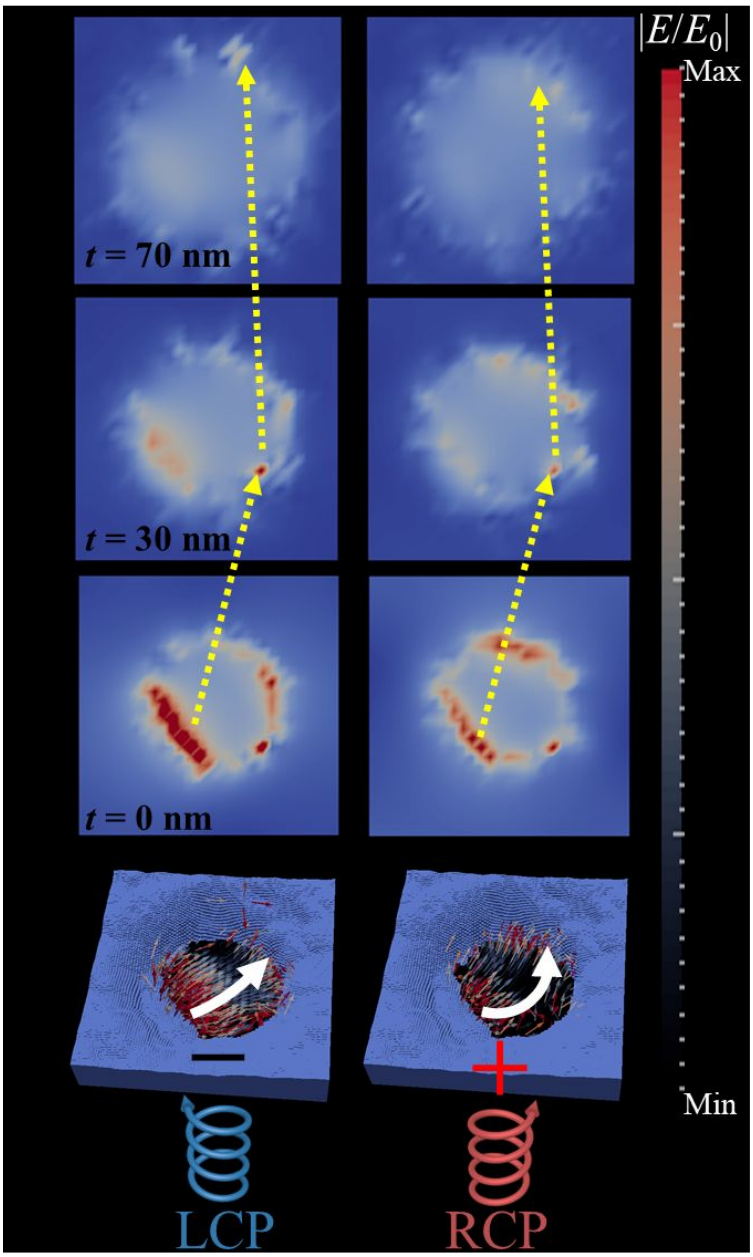

Figure 4. The normalized electric field distributions $|E/E_0|$ of the LH-CNA at three interfaces, t = 0 (Ag/glass interface), 30, and 70 (Ag/air interface) nm, excited by an LCP and RCP incident light at λ_5 = 764 nm, respectively. The dashed yellow arrows indicate the change of the maximum local electric fields.

In addition, the optical rotation of the LH-CNA sample was probed under a linearly polarized light at normal incidence, as shown in **Figure 5A**. We find that the rotation of linear polarized light depends on the relative in-plane angle α between the polarization direction of the incident light and the orientation of the nanohole (see inset of **Figure 5A** and the polar plots of $\Delta\alpha$ in **Figure S5**). This is because the unit cell of the LH-CNAs does not possess a perfect in-plane rotational symmetry and induces a linear birefringence (LB). A significant optical rotation $\Delta\alpha$ = - 9.5° is observed at $\lambda \approx 696$ nm (the red curve in **Figure 5A**), which is about five times higher than the optical rotation with the linear birefringence effect (~ 2°) of gammadion grating.[44] Note that $T_R(\lambda)$ and $T_L(\lambda)$ are perfectly balanced around 696 nm (dashed black curve in **Figure 5A**), *i.e.*, $T_R(\lambda) = T_L(\lambda)$, or $CD(\lambda) = 0$, as indicated by the vertical dotted blue line in **Figure 5A**. Thus, $\Delta\alpha$ at $\lambda \approx 696$ nm is a pure optical rotation, which is exclusively induced by LB without CD. The max $\Delta\alpha$ = - 9.5° translates to a polarization rotation power of up to 94° per free space wavelength according to $\frac{\Delta\alpha \times \lambda}{t}$.[63] The actual optical activity is quantified as the averaged $\Delta\alpha$ with respect to the azimuthal angle, showing a maximum of 2.5° at λ = 670 nm (**Figure 5B**), which translates to approximately 24° per λ. The averaged $\Delta\alpha$ = 2.5° of CNA is about two times higher than that (~ 1°) of gammadion grating. There are other wavelengths at 775 nm and around 600 nm where CD is close to zero, as shown in **Figure 2F**. The averaged $\Delta\alpha$ is also close to zero at these wavelengths, showing little rotation power. Note that the averaged $\Delta\alpha$ is close to zero at the wavelengths around 750 nm and 800 nm, while the experimental CD peaks/valleys λ_1 = 743 nm and λ_5 = 822 nm appear at these wavelengths. This indicates that the major CD signals are only

induced by SPP and LSPR, not the linear birefringence. Although CNA is asymmetric, the LB and CD effects can be separated at the key spectral features (peaks/valleys), making its application simple and straightforward. The optical activity originates from the difference of the indices of refraction $n_R(\lambda)$ and $n_L(\lambda)$ by $\Delta\alpha = \pi H[n_R(\lambda) - n_L(\lambda)]/\lambda$. The measured average index contrast $\Delta n = n_R(\lambda) - n_L(\lambda)$ at $\lambda = 670$ nm is 0.13, showing the ability of tuning the effective refractive index. In addition, the chiral responses of the CNAs hardly change in different domains (lattice orientation), demonstrating domain-independent chirality or homogeneity/uniformity of the substrate (**Figure S6**). No alignment procedures are required for fabricating uniform and large area CNAs. This fabrication process is much simpler and more efficient compared with previous reports based on SSL.[48-49] The strong and consistent optical activity and CD response of the large-area CNAs offer great potentials in polarization converter and chiral sensing.

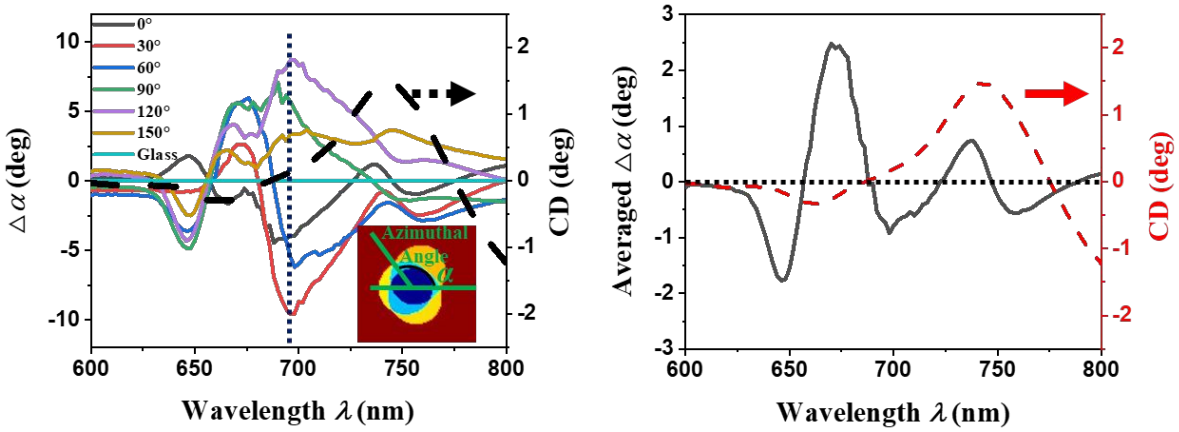

Figure 5. (A) The optical rotation $\Delta\alpha$ of the LH-CNA sample at $\alpha = 0^o$, 30^o, 60^o, 90^o, 120^o, and 150^o. The inset shows the definition of in-plane angle α. The $\Delta\alpha$ of the bare glass substrate is also shown with the values of zero. The initial azimuthal angle (0^o) is chosen arbitrarily. The CD

spectrum of LH-CNA is shown by the dashed black curve. The vertical dotted blue line indicates the values of $\Delta\alpha$ and CD at λ = 696 nm. (B) The plot of the average $\Delta\alpha$ of the LH-CNA based on the spectra in (A). The CD spectrum of LH-CNA is shown by the dashed red curve. The dotted line indicates $\Delta\alpha$ and CD = 0.

2.3 Chiral Sensing

One of the main advantages for chiral metamaterials is the possibility of producing superchiral fields for sensitively detecting chiral molecules. According to Tang and Cohen, a parameter termed as the optical chirality C can be used to characterize the local density of the chirality electromagnetic field, [64]

$$C = \frac{\varepsilon_0}{2}\boldsymbol{E}\cdot\nabla\times\boldsymbol{E} + \frac{1}{2\mu_0}\boldsymbol{B}\cdot\nabla\times\boldsymbol{B}, \quad (1)$$

where ε_0 and μ_0 are the permittivity and permeability of free space, and $\boldsymbol{E}$ and $\boldsymbol{B}$ are the local electric and magnetic fields. Based on the AFM model, the normalized optical chirality distribution C/C_0 at the Ag/air and Ag/glass interfaces for circularly polarized plane waves at λ_5 = 764 nm are presented in **Figure 6A**, where C_0 is optical chirality calculated used the free-space propagated $\boldsymbol{E}_0$ and $\boldsymbol{B}_0$ values. Clearly inside the nanohole of the Ag/air interface and at the hole edge of the Ag/glass interface, very strong superchiral fields are excited. The C/C_0 values are almost all positive under LCP light incidence and are negative under RCP light incidence, and the maximum enhancement can reach as high as 50. The enhancement could be larger if smaller mesh size was used in the calculation. The calculated C/C_0 distributions of the SPP peak at λ_1 = 739 nm are shown in **Figure S7** and exhibit the similar results to that of **Figure 6A**. It is

expected that such a strong superchiral field could result in a distinguished difference in index of refraction due to chiral molecules for the LCP or RCP incident light, *i.e.*, the CNA structures can be used for highly sensitive chiral molecule detection.

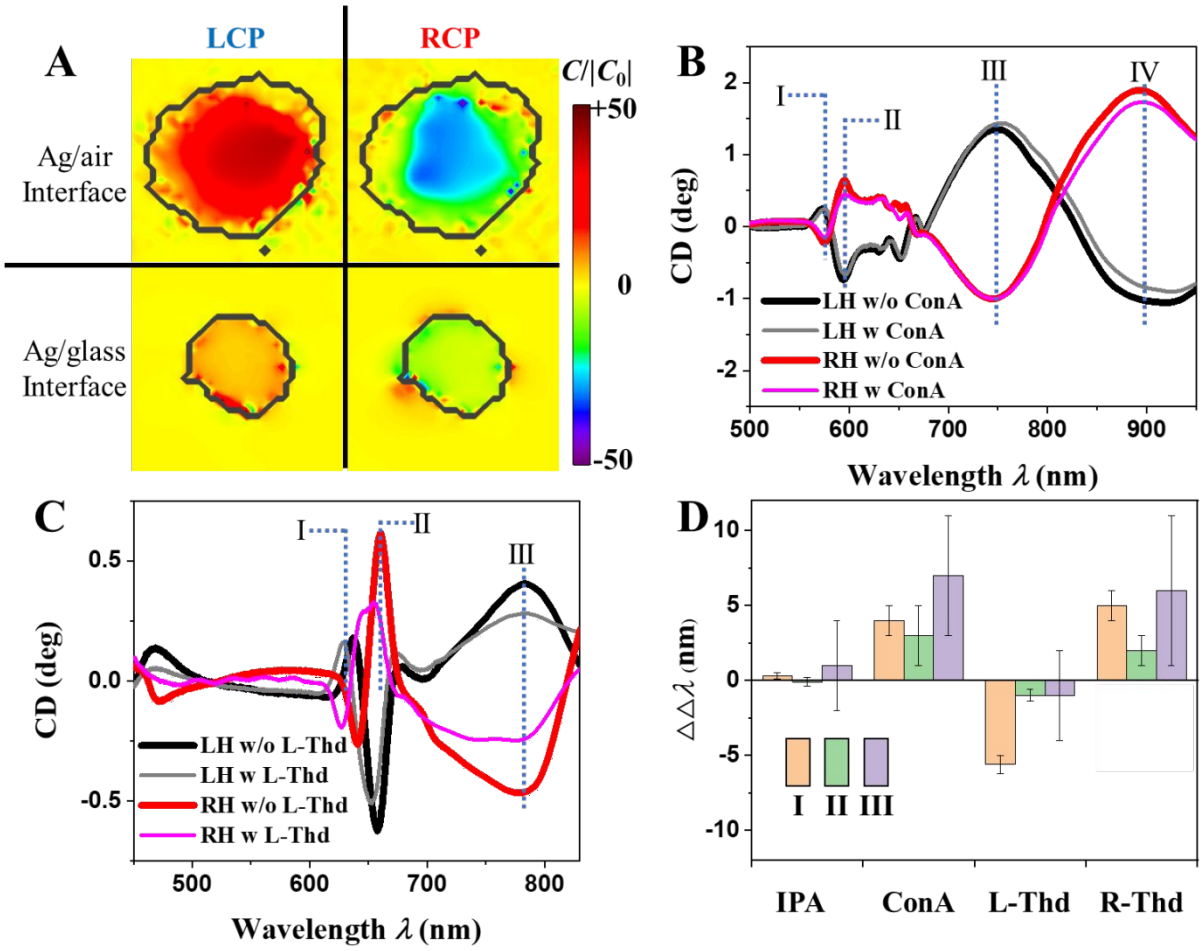

Figure 6. (A) The normalized superchiral field $|C/C_0|$ maps of the LH-CNAs excited by LCP and RCP incident light at λ_5 = 764 nm at the Ag/air and Ag/glass interface. The black curves show the outlines of the nanoholes. (B) The CD spectra of the LH- and RH-CNAs with and without ConA. The four main modes are labeled as I, II, III, and IV, respectively. (C) The CD spectra of the LH- and RH-CNAs with and without L-ThD. The three main modes are labeled as I, II, and III,

corresponding to those in (B). (D) The plot of $\Delta\Delta\lambda$ for ConA, L-Thd, and R-Thd. Also shown are the effectively zero $\Delta\Delta\lambda$ values obtained from the (achiral) IPA solvent.

To demonstrate this application, we have applied the CNAs to detect the chiral structures of biomolecules and drug molecules. The structural chirality of the molecules near the surfaces of the CNAs is determined by the dissymmetry factor ($\Delta\Delta\lambda = \Delta\lambda_L - \Delta\lambda_R$), where $\Delta\lambda_L$ and $\Delta\lambda_R$ are the shifts of the CD spectral peaks (or valleys) of the LH-CNA and RH-CNA samples after targeted chiral molecules are adsorbed on the sample. First, we applied the CNAs enantiomers (their CD response are shown in **Figure 2G**) to detect Concanavalin A (ConA), which is a chiral protein of high β-sheet content.[13, 65] When the sample was immersed in the buffer solution ($n \approx 1.33$), four modes appear in the CD spectra, which correspond to the mode I, II, III and IV in **Figure 6B**. The modes III and IV correspond to the LSPR (λ_5) and SPP (λ_1) modes in **Figure 2F**, but have a significant red shift, which can be identified from their original transmission spectra (**Section SVIII in SI)**. Note that though λ_1 is assigned as the SPP peak at the Ag/glass interface, it still shows a large red-shift. This is because the excitation of the EOT peak is not just the function of one interface, but also the coupling between the Ag/air and Ag/glass interfaces. Also due to the increase of n, new modes I and II appear, which are not observed in the CD spectra in air. The larger n leads to better match (coupling) between the bottom glass and top surface.[66] Higher-order LSPR and SPP could become significant and result in new emerging modes I and II. It is hard to have an exact assignment for the modes I and II because of the possible overlap of the

different plasmon resonance modes.[67] The FDTD calculations provide less information on modes I and II because they are so weak and sensitive to the variations of the structure and calculation conditions, while the experimental results are convincing considering the modes I and II can be perfectly mirrored for the enantiomers and can be reproduced well for different sample locations and batches of samples, even in different solvent (**Figure S9** and **Figure S10**). Based on the discussion for **Figure 3** and **Figure 4**, we believe that the mode II is induced by SPP, while high-order LSPR could be responsible for mode I.

When achiral molecule of isopropanol (IPA) was tested (see **Section SVII** of **SI**), the CD spectra shows the same four modes at the similar wavelengths as those in buffer solution, because *n* does not change much (from 1.33 to 1.36). The assignment of the modes in **Figure S8B** and **Figure 6B** is still applied. The modes I, II, III, and IV all shift to red, while $\Delta\Delta\lambda$ has a nearly zero value (0.3 ± 0.2 nm, -0.1 ± 0.3 nm, and 1 ± 3 nm) as expected for achiral molecules (**Figure S10** and **Figure 6D**). The mode IV is not studied because their broad band-width would lead to large errors. **Figure 6B** shows the CD spectra of the CNA enantiomers before (in buffer solution) and after the adsorption of a trace amount (1 mg/mL, corresponding to ≈ 250 pg detected in the experiments[65]) of ConA. The CD spectra of the LH-CNA and RH-CNA samples both shift to red after absorbing ConA (see discussion in **Section SVIII** of **SI**), but showing different values. The $\Delta\Delta\lambda$ for the modes I, II, and III is 4 ± 1 nm, 3 ± 2 nm, and 7 ± 4 nm, respectively, which is comparable to those of the state-of-the-art plasmonic metamaterials,[13, 52, 65], *i.e.*, the CNAs can detect the chiral biomolecules at the pg level. The error bar was obtained

by statistically analyzing six measurements at different locations. For the detection mechanism, it was claimed that chiral molecules introduce asymmetric modification of local refractive index and thus asymmetric values of $\Delta\lambda_L$ and $\Delta\lambda_R$.[64] With their enhanced and compact superchiral fields generated by circularly polarized illumination, the CNAs enable the enantiodiscrimination of molecules with the higher sensitivity than the conventional techniques.[16, 68] However, the detection mechanism is still under debate since the intermediation of chiral electric and magnetic modes in a plasmonic nanostructure by biomolecules may also lead to the detection of chirality in molecules.[69]

Detection of structural chirality is of crucial importance to medical industry because the enantiomers of many chiral drugs have harmful effects on human body. One example is thalidomide. R-thalidomide (R-Thd) is an effective painkiller, while its 'evil twin' (L-Thd) can cause deformity of newly born babies.[1] Although plasmonic super chiral fields have been successfully applied to detect the chiral structures of proteins, it has remained challenging to detect the structural handedness of drug molecules due to their small size. An effective sensing of small chiral molecules requires the strong enhancement of optical chirality, which can be obtained by 3D chiral structures with highly compact hot spots.[70] We have succeeded in distinguishing R-Thd and its "evil twin" at the pg level based on the CNAs. The original transmission spectra and assignment of the modes can be found in **Section SX**. The $T_L(\lambda)$ and $T_R(\lambda)$ of the LH-RNA after adsorbing R-ThD and L-ThD are very similar and corresponding plasmonic peaks/valleys significantly shift to red compared to those in air and ConA. The red

shift is due to that n of the surrounding environment (DMSO, $n \approx 1.48$) is much larger. There are still distinct λ_1 and λ_5 CD peak/valley, which corresponds to the modes IV and III, respectively. The corresponding CD spectra for both the L-Thd adsorbed on both the LH-CNA and RH-CNA enantiomers are shown in **Figure 6C**. The modes I, II, and III are still well identified, which shift to blue compared to those in only DMSO (w/o L-Thd). The three modes can also be clearly seen when R-Thd was adsorbed on the samples (**Figure S11D**), while show red shift compared with those in DMSO (w/o R-Thd). The $\Delta\Delta\lambda$ of CD spectra for the LH- and RH-CNAs after the adsorbing of the R-ThD and L-ThD (2 mg/mL) are shown in **Figure 6D**. The $\Delta\Delta\lambda$ for L-ThD has negative values of - 5.6 ± 0.6 nm, - 1.1 ± 0.4, and - 1 ± 3 nm for modes I, II, and III, respectively. In contrast, for R-ThD, the $\Delta\Delta\lambda$ has positive values of 5 ± 1 nm, 2 ± 1 nm, and 6 ± 5 nm for the modes I, II, and III, respectively. The mode II shows reasonable performance for chiral sensing, while the error for the mode III is large due to the broad peak/valley. The mode I shows the best overall sensing performances with the highest $\Delta\Delta\lambda$ and smallest error. The mode I is considered to be excited by high-order LSPR, which has small radiative/coupling loss. This leads to the higher sensitivity, narrower bandwidth, and better quality.[71, 72]

The dissymmetric responses to chiral molecules can be well identified at pg level. This sensitivity is in the same level with those fabricated by EBL[16] and higher than those ($\Delta\Delta\lambda_{ConA}$ = 2.5 nm and $\Delta\Delta\lambda_{ThD} < 1$ nm) fabricated by soft lithography techniques under the same measuring conditions.[52] The excellent sensing capability of the CNAs is attributed to the compact hot spots in the nanoholes, which can be easily accessible to the detection molecules with a facile

penetration.[73] The CNAs can be fabricated in a large area (here we can produce them on 1"×3" glass slides), which can be easily made into on-chip sensing devices. The CNAs also show high uniformity and excellent reproducibility of as demonstrated by the measurements from different sample locations, batches of samples, and solvents (see **Figure S6**, **Figure S9,** and **Figure S10**). In addition, the on-chip sensors based on NAs have been well studied with mature techniques.[74, 75] With above advantages the CNAs are ready to be integrated for on-chip sensing platform for detecting chiral molecules.

3. Conclusion

In summary, a novel model of chiral metamaterials – chiral nanohole array – is introduced in this work. The chirality and optical activity of CNAs are larger compared to most of other planar chiral metamaterials, which is due to the structure induced rotation of SPP and LSPR on the interhole film and in the nanoholes, respectively. Strong superchiral fields are excited and show sensitive dissymmetry responses to chiral proteins and molecules at the picogram level, which is comparable to the state-of-the-art plasmonic metamaterial. Although the chiral performances are not the best among previous reports, the fabrication processes of the CNAs are much simpler, lower-cost, and higher-throughput. The CNAs have an ultrathin thickness and high transmission, showing significant advantages for practical ultracompact devices of polarization converter and chiral sensors. The chiral performances of the CNAs are promising and could be further improved by inserting dielectric layers between each nanohole layer and by optimizing the

structural parameters. The nanohole array with EOT is a well-studied plasmonic model for optical filter, structural color, sensors, *et. al.* The strategy of introducing chiral elements in nanohole arrays will lead to facile explanations of the chirality and easy realization of highly integrated devices based on the existing theory and experiences.

4. Experimental Section

Materials: 500 nm PS nanospheres (Polyscience, Lot# 679675 and Lot# 687640) and ethanol (Sigma-Aldrich, 98%) were used to form the colloid monolayers on cleaned glass slides (Gold Seal, Part# 3010). Prior to monolayer formation, the glass substrates were cleaned by sulfuric acid (Fisher Scientific, 98%), ammonium hydroxide (Fisher Scientific, 98%), and hydrogen peroxide (Fisher Scientific, 30%). Silver pellets (Plasmaterials, 99.99%) were used as the evaporation source. Toluene (Fisher Scientific, 99.8%), acetone (Fisher-Scientific, 99.8%), and ethanol were applied subsequently to remove PS nanosphere residue after deposition. Concanavalin A from canavalia ensiformis (Sigma-Aldrich, Type IV-S), and R- and L-thalidomide (Sigma-Aldrich, > 98%) were used for protein and drug sensing measurements. Trizma hydrochloride solution (Sigma-Aldrich, 1M) and dimethyl sulfoxide (Sigma-Aldrich) were used as buffer solutions for ConA and L-Thd/R-Thd, respectively. Deionized (DI) water (18MΩ cm) was used throughout the experiments. All chemicals and materials were used without further purification.

Fabrication of CNAs: The PS nanosphere monolayers were prepared on glass substrates by an

air−water interface method. Details can be found elsewhere.[76] The size of the PS nanospheres of the monolayer was then reduced to ~ 200 nm by a reactive ion etching (RIE) in a Trion technology Phantom III RIE/ICP system. The etching conditions were set to be: the processing pressure of 40 mTorr, the oxygen flow of 10 sccm, the ICP power of 25 W, the RF power of 10 W, and the etching time of 450 s. Ag nanostructures were prepared using a custom-built electron beam deposition system with a deposition configuration shown in Figure 1A. The glass substrates with etched nanospheres were mounted on a substrate holder with two motors to control the polar and azimuthal rotations. The chamber was evacuated to a base pressure of 1×10^{-6} Torr and then maintained below 5×10^{-6} Torr during the Ag deposition. The Ag deposition rate was monitored by a quartz crystal microbalance and measured to be 0.1 nm/s. During the deposition, the deposition angle θ, relative to the substrate surface normal and the azimuthal angle φ were programed to change by (θ, φ) = (10°, 0°) (initial φ), (20°, ± 120°), and (30°, ± 240°). For each fixed azimuthal angle, the total deposited Ag thickness was 30 nm. When the deposition was completed, the substrates were allowed to return to room temperature over a period of several hours inside the chamber. Once removed from the chamber, the PS nanospheres were removed using a Scotch tape. The PS residue on the samples was further removed by soaking the samples successively in toluene, acetone, and ethanol for 3 min each. The samples were then dried under a flow of N_2, and either tested immediately or stored in an argon environment.

Structure and Finite-Difference Time-Domain (FDTD) Calculations: The CNA structures

formed by the etched monolayer and deposition configuration described above were predicted by an in-house MATLAB program.[77] This program simulated the deposition process by projecting Ag vapor through the etched monolayer mask at desired values of θ and φ, but does not take into account of the shadowing effect of the thin film deposited on the PS nanospheres.

A commercial software package (FDTD Solutions v 8.19.1584, Lumerical Solutions Inc.) was used to calculate the transmission spectra, current densities, electric field distributions, and superchiral field distributions of the CNAs. The CNA models predicted by the MATLAB program and obtained from the AFM images were imported as the calculation models. Two or three rectangular unit cells were set as the calculation area with periodic boundary conditions. The circular polarization was generated by two sources polarized along orthogonal axes with differential phase of $\pi/2$. Perfectly matched layer boundary conditions were used on the top and bottom surfaces of the calculation domain. Monitors of "frequency-domain field and power", "frequency domain field profile", and current analysis group were set up to calculate the transmission spectra, localized electric field distributions, and current distributions, respectively.

Morphological and Optical Characterizations: The surface morphology of the samples was characterized by an atomic force microscope (AFM, Park NX20). Experimental spectra under circularly polarized incident lights were measured by a custom spectroscopic microscope system with a spot size of 200 μm over a wavelength range of 450–950 nm. Details of the optical setup can be seen in Ref.[78] The CD spectra are measured in transmission with the normal of substrate.

Protein and Drug Measurements: The CNAs on glass substrate were placed inside a quartz

cuvette, sealed with a plastic cap to avoid leaking during measurement. The thickness of the fluid layer above the film is 9 mm. For ConA measurement, Tris/HCl (10×10^{-3} M, pH = 7.4) was utilized as a buffer solution. The concentration of ConA was 1 mg/mL. For L-Thd and R-Thd measurements, dimethyl sulfoxide (DSMO) from Sigma-Aldrich was used as buffer solution. The concentration of L-Thd and R-Thd solutions were 2 mg/mL. All the drug solutions were prepared right before each sensing measurement. The error bars were achieved from six measurements at different sample locations.

Conflict of interest

There are no conflicts to declare

Acknowledgements

[∇] B.A and H.M.L contributed equally. This work was supported by the National Science Foundation under Grant no. CMMI-1435309 and ECCS-1611330.

References

1. V. K. Valev, J. J. Baumberg, C. Sibilia and T. Verbiest, *Adv Mater*, 2013, **25**, 2517-2534.
2. L. D. Barron, *Molecular light scattering and optical activity*, Cambridge University Press, 2009.
3. Y.-H. Chen, J. T. Yang and H. M. Martinez, *Biochemistry*, 1972, **11**, 4120-4131.
4. Y. Luo, C. Chi, M. Jiang, R. Li, S. Zu, Y. Li and Z. Fang, *Adv Opt Mater*, 2017, **5**, 1700040.
5. J. Pendry, *Science*, 2004, **306**, 1353-1355.
6. S. Zhang, Y.-S. Park, J. Li, X. Lu, W. Zhang and X. Zhang, *Phys Rev Lett*, 2009, **102**, 023901.
7. J. K. Gansel, M. Thiel, M. S. Rill, M. Decker, K. Bade, V. Saile, G. von Freymann, S. Linden and M. Wegener, *Science*, 2009, **325**, 1513-1515.
8. Y. Zhao, M. Belkin and A. Alù, *Nat Commun*, 2012, **3**, 870.
9. S. Zu, T. Y. Han, M. L. Jiang, F. Lin, X. Zhu and Z. Y. Fang, *Acs Nano*, 2018, **12**, 3908-

3916.
10. S. Zu, T. Y. Han, M. L. Jiang, Z. X. Liu, Q. Jiang, F. Lin, X. Zhu and Z. Y. Fang, *Nano Lett*, 2019, **19**, 775-780.
11. T. Y. Han, S. Zu, Z. W. Li, M. L. Jiang, X. Zhu and Z. Y. Fang, *Nano Lett*, 2018, **18**, 567-572.
12. A. Kuzyk, R. Schreiber, H. Zhang, A. O. Govorov, T. Liedl and N. Liu, *Nat Mater*, 2014, **13**, 862-866.
13. S. Eslami, J. G. Gibbs, Y. Rechkemmer, J. van Slageren, M. Alarcon-Correa, T. C. Lee, A. G. Mark, G. L. J. A. Rikken and P. Fischer, *Acs Photonics*, 2014, **1**, 1231-1236.
14. S. P. Rodrigues, S. F. Lan, L. Kang, Y. H. Cui and W. S. Cai, *Adv Mater*, 2014, **26**, 6157-6162.
15. V. K. Valev, *Langmuir*, 2012, **28**, 15454-15471.
16. E. Hendry, T. Carpy, J. Johnston, M. Popland, R. V. Mikhaylovskiy, A. J. Lapthorn, S. M. Kelly, L. D. Barron, N. Gadegaard and M. Kadodwala, *Nat Nanotechnol*, 2010, **5**, 783-787.
17. R. Tullius, G. W. Platt, L. Khosravi Khorashad, N. Gadegaard, A. J. Lapthorn, V. M. Rotello, G. Cooke, L. D. Barron, A. O. Govorov, A. S. Karimullah and M. Kadodwala, *Acs Nano*, 2017, **11**, 12049-12056.
18. S. Lee, J. H. Kang, S. Yoo and Q. H. Park, *Sci Rep-Uk*, 2018, **8**, 8406.
19. C. Hao, L. Xu, H. Kuang and C. Xu, *Adv Mater*, 2019, 1802075.
20. M. Qiu, L. Zhang, Z. X. Tang, W. Jin, C. W. Qiu and D. Y. Lei, *Adv Funct Mater*, 2018, **28**, 1803147.
21. Y. D. Hou, H. M. Leung, C. T. Chan, J. L. Du, H. L. W. Chan and D. Y. Lei, *Adv Funct Mater*, 2016, **26**, 7807-7816.
22. A. Passaseo, M. Esposito, M. Cuscuna and V. Tasco, *Adv Opt Mater*, 2017, **5**, 1601079.
23. M. Kadic, G. W. Milton, M. van Hecke and M. Wegener, *Nat Rev Phys*, 2019, **1**, 198–210.
24. S. Zu, Y. J. Bao and Z. Y. Fang, *Nanoscale*, 2016, **8**, 3900-3905.
25. V. A. Fedotov, A. S. Schwanecke, N. I. Zheludev, V. V. Khardikov and S. L. Prosvirnin, *Nano Lett*, 2007, **7**, 1996-1999.
26. X. Yang, M. Li, Y. D. Hou, J. L. Du and F. Gao, *Opt Express*, 2019, **27**, 6801-6814.
27. W. M. Ye, X. D. Yuan, C. C. Guo, J. F. Zhang, B. A. Yang and S. Zhang, *Phys Rev Appl*, 2017, **7**, 054003.
28. Y. Li, Y. J. Xu, M. L. Jiang, B. W. Li, T. Y. Han, C. Chi, F. Lin, B. Shen, X. Zhu, L. H. Lai and Z. Y. Fang, *Phys Rev Lett*, 2019, **123**, 213902.
29. M. Hentschel, V. E. Ferry and A. P. Alivisatos, *Acs Photonics*, 2015, **2**, 1253-1259.
30. Y. Cui, L. Kang, S. Lan, S. Rodrigues and W. Cai, *Nano Lett*, 2014, **14**, 1021-1025.
31. M. Decker, R. Zhao, C. Soukoulis, S. Linden and M. Wegener, *Opt Lett*, 2010, **35**, 1593-1595.
32. A. Radke, T. Gissibl, T. Klotzbücher, P. V. Braun and H. Giessen, *Adv Mater*, 2011, **23**,

3018-3021.
33. J. Kaschke, L. Blume, L. Wu, M. Thiel, K. Bade, Z. Yang and M. Wegener, *Adv Opt Mater*, 2015, **3**, 1411-1417.
34. C. Vieu, F. Carcenac, A. Pepin, Y. Chen, M. Mejias, A. Lebib, L. Manin-Ferlazzo, L. Couraud and H. Launois, *Appl Surf Sci*, 2000, **164**, 111-117.
35. A. Selimis, V. Mironov and M. Farsari, *Microelectron Eng*, 2015, **132**, 83-89.
36. A. Kuzyk, R. Schreiber, Z. Fan, G. Pardatscher, E.-M. Roller, A. Högele, F. C. Simmel, A. O. Govorov and T. Liedl, *Nature*, 2012, **483**, 311.
37. B. M. Maoz, Y. Chaikin, A. B. Tesler, O. Bar Elli, Z. Y. Fan, A. O. Govorov and G. Markovich, *Nano Lett*, 2013, **13**, 1203-1209.
38. F. Leroux, M. Gysemans, S. Bals, K. J. Batenburg, J. Snauwaert, T. Verbiest, C. Van Haesendonck and G. Van Tendeloo, *Adv Mater*, 2010, **22**, 2193-2197.
39. K. Hur, Y. Francescato, V. Giannini, S. A. Maier, R. G. Hennig and U. Wiesner, *Angew Chem Int Edit*, 2011, **50**, 11985-11989.
40. S. Vignolini, N. A. Yufa, P. S. Cunha, S. Guldin, I. Rushkin, M. Stefik, K. Hur, U. Wiesner, J. J. Baumberg and U. Steiner, *Adv Mater*, 2012, **24**, Op23-Op27.
41. Z. Y. Wang, B. Ai, Z. W. Zhou, Y. D. Guan, H. Mohwald and G. Zhang, *Acs Nano*, 2018, **12**, 10914-10923.
42. Y. Z. He, G. K. Larsen, W. Ingram and Y. P. Zhao, *Nano Lett*, 2014, **14**, 1976-1981.
43. Y. He, G. Larsen, X. Li, W. Ingram, F. Chen and Y. Zhao, *Adv Opt Mater*, 2015, **3**, 342-346.
44. M. Kuwata-Gonokami, N. Saito, Y. Ino, M. Kauranen, K. Jefimovs, T. Vallius, J. Turunen and Y. Svirko, *Phys Rev Lett*, 2005, **95**, 227401.
45. R. Tullius, G. W. Platt, L. K. Khorashad, N. Gadegaard, A. J. Lapthorn, V. M. Rotello, G. Cooke, L. D. Barron, A. O. Govorov, A. S. Karimullah and M. Kadodwala, *Acs Nano*, 2017, **11**, 12049-12056.
46. R. Ogier, Y. Fang, M. Svedendahl, P. Johansson and M. Käll, *Acs Photonics*, 2014, **1**, 1074-1081.
47. V. K. Valev, N. Smisdom, A. V. Silhanek, B. De Clercq, W. Gillijns, M. Ameloot, V. V. Moshchalkov and T. Verbiest, *Nano Lett*, 2009, **9**, 3945-3948.
48. T. Narushima, S. Hashiyada and H. Okamoto, *Acs Photonics*, 2014, **1**, 732-738.
49. K. Dietrich, C. Menzel, D. Lehr, O. Puffky, U. Hübner, T. Pertsch, A. Tünnermann and E.-B. Kley, *Appl Phys Lett*, 2014, **104**, 193107.
50. B. Bai, J. Laukkanen, A. Lehmuskero and J. Turunen, *Phys Rev B*, 2010, **81**, 115424.
51. A. V. Kondratov, M. V. Gorkunov, A. N. Darinskii, R. V. Gainutdinov, O. Y. Rogov, A. A. Ezhov and V. V. Artemov, *Phys Rev B*, 2016, **93**, 195418.
52. Z. L. Wu and Y. B. Zheng, *Adv Opt Mater*, 2017, **5**, 1700034.
53. Z. L. Wu, X. D. Chen, M. S. Wang, J. W. Dong and Y. B. Zheng, *Acs Nano*, 2018, **12**, 5030-5041.

54. T. W. Ebbesen, H. J. Lezec, H. Ghaemi, T. Thio and P. A. Wolff, *Nature*, 1998, **391**, 667.
55. C. Genet and T. W. Ebbesen, in *Nanoscience And Technology: A Collection of Reviews from Nature Journals*, World Scientific, 2010, pp. 205-212.
56. S. Reyntjens and R. Puers, *J Micromech Microeng*, 2001, **11**, 287.
57. B. Ai and Y. P. Zhao, *Nanophotonics-Berlin*, 2019, **8**, 1-26.
58. C. J. Kim, A. Sanchez-Castillo, Z. Ziegler, Y. Ogawa, C. Noguez and J. Park, *Nat Nanotechnol*, 2016, **11**, 520–524.
59. R. W. Wood, *Phys Rev*, 1935, **48**, 928.
60. L. Martin-Moreno, F. Garcia-Vidal, H. Lezec, K. Pellerin, T. Thio, J. Pendry and T. Ebbesen, *Phys Rev Lett*, 2001, **86**, 1114.
61. W. C. Johnson, *Annu Rev Biophys Bio*, 1988, **17**, 145-166.
62. Z. Y. Fan and A. O. Govorov, *Nano Lett*, 2010, **10**, 2580-2587.
63. Y. H. Cui, L. Kang, S. F. Lan, S. Rodrigues and W. S. Cai, *Nano Lett*, 2014, **14**, 1021-1025.
64. Y. Tang and A. E. Cohen, *Phys Rev Lett*, 2010, **104**, 163901.
65. A. S. Karimullah, C. Jack, R. Tullius, V. M. Rotello, G. Cooke, N. Gadegaard, L. D. Barron and M. Kadodwala, *Adv Mater*, 2015, **27**, 5610-5616.
66. A. Krishnan, T. Thio, T. Kim, H. Lezec, T. Ebbesen, P. Wolff, J. Pendry, L. Martin-Moreno and F. Garcia-Vidal, *Opt Commun*, 2001, **200**, 1-7.
67. S. H. Lee, K. C. Bantz, N. C. Lindquist, S.-H. Oh and C. L. Haynes, *Langmuir*, 2009, **25**, 13685-13693.
68. R. Tullius, A. S. Karimullah, M. Rodier, B. Fitzpatrick, N. Gadegaard, L. D. Barron, V. M. Rotello, G. Cooke, A. Lapthorn and M. Kadodwala, *J Am Chem Soc*, 2015, **137**, 8380-8383.
69. C. Jack, A. S. Karimullah, R. Leyman, R. Tullius, V. M. Rotello, G. Cooke, N. Gadegaard, L. D. Barron and M. Kadodwala, *Nano Lett*, 2016, **16**, 5806-5814.
70. M. Schäferling, D. Dregely, M. Hentschel and H. Giessen, *Phys Rev X*, 2012, **2**, 031010.
71. C. Wu, A. B. Khanikaev, R. Adato, N. Arju, A. A. Yanik, H. Altug and G. Shvets, *Nat Mater*, 2012, **11**, 69.
72. J. Zhao, C. Zhang, P. V. Braun and H. Giessen, *Adv Mater*, 2012, **24**, OP247-OP252.
73. A. G. Brolo, *Nature Photonics*, 2012, **6**, 709.
74. R. Gordon, A. G. Brolo, D. Sinton and K. L. Kavanagh, *Laser Photonics Rev*, 2010, **4**, 311-335.
75. C. Escobedo, *Lab on a Chip*, 2013, **13**, 2445-2463.
76. W. M. Ingram, C. Q. Han, Q. J. Zhang and Y. P. Zhao, *J Phys Chem C*, 2015, **119**, 27639-27648.
77. G. K. Larsen, Y. Z. He, W. Ingram and Y. P. Zhao, *Nano Lett*, 2013, **13**, 6228-6232.
78. Y. Z. He, K. Lawrence, W. Ingram and Y. P. Zhao, *Acs Photonics*, 2015, **2**, 1246-1252.

ToC figure

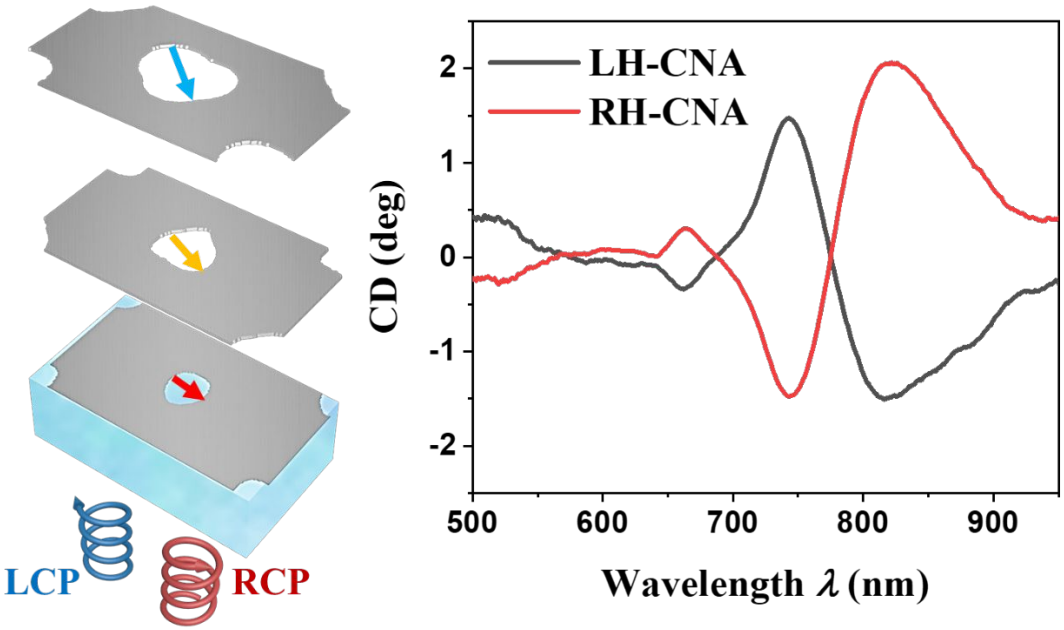

Ultra-thin chiral nanohole array films are fabricated by a simple and efficient shadow sphere lithography (SSL) method and achieve label-free enantiodiscrimination of biomolecules and drug molecules at the picogram level.